

Title: Label-free segmentation from cardiac ultrasound using self-supervised learning

Authors: Danielle L. Ferreira PhD^a, Zaynaf Salaymang RDCS^b, Rima Arnaout MD^{c*}

^aDepartment of Medicine, Division of Cardiology
Bakar Computational Health Sciences Institute
University of California, San Francisco

^bDepartment of Medicine, Division of Cardiology
University of California, San Francisco

^cDepartment of Medicine, Division of Cardiology
Bakar Computational Health Sciences Institute
Chan Zuckerberg Biohub Intercampus Research Award Investigator
Center for Intelligent Imaging
Department of Radiology
Biological and Medical Informatics Graduate Program
University of California, San Francisco

* Corresponding Author

Sources of Funding

D.F. and R.A. were supported by the National Institutes of Health (R01HL150394) to R.A. R.A. is additionally supported by the Department of Defense (PR181763) and the Chan Zuckerberg Biohub. Work is subject to UCSF Disclosure SF2022-263. All authors declare that they have no conflicts of interest.

Address for Correspondence:

Rima Arnaout MD
University of California, San Francisco
Email: rima.arnaout@ucsf.edu

Abstract

Background: Segmentation and measurement of cardiac chambers is critical in echocardiography but is also laborious and poorly reproducible. Neural networks can assist, but supervised approaches require the same laborious manual annotations, while unsupervised approaches have fared poorly in ultrasound to date.

Objectives: We built a pipeline for self-supervised (no manual labels required) segmentation of cardiac chambers, combining computer vision, clinical domain knowledge, and deep learning.

Methods: We trained on 450 echocardiograms (145,000 images) and tested on 8,393 echocardiograms (4,476,266 images; mean age 61 years, 51% female), using the resulting segmentations to calculate structural and functional measurements. We also tested our pipeline against external images from an additional 10,030 patients (20,060 images) with available manual tracings of the left ventricle.

Results: r^2 between clinically measured and pipeline-predicted measurements were similar to reported inter-clinician variation for LVESV and LVEDV (pipeline vs. clinical $r^2= 0.74$ and $r^2=0.65$, respectively), LVEF and LV mass ($r^2= 0.46$ and $r^2=0.54$), left and right atrium volumes ($r^2=0.7$ and $r^2=0.6$), and right ventricle area ($r^2=0.47$). When binarized into normal vs. abnormal categories, average accuracy was 0.81 (range 0.71-0.95). A subset of the test echocardiograms ($n=553$) had corresponding cardiac MRI; correlation between pipeline and CMR measurements was similar to that between clinical echocardiogram and CMR. Finally, in the external dataset, our pipeline accurately segments the left ventricle with an average Dice score of 0.83 (95% CI 0.83).

Conclusions: Our results demonstrate a human-label-free, valid, and scalable method for segmentation from ultrasound, a noisy but globally important imaging modality.

Keywords: deep learning, machine learning, semantic segmentation, self-supervised learning, cardiovascular imaging, ultrasound, echocardiography.

Introduction

Quantification of cardiac chamber size, mass, and function in echocardiography are critical to diagnosis, prognosis, and management¹. However, quantification is laborious, requiring several manual annotations per view, per exam. Even when performed by experts, manual annotations can be susceptible to inter- and intra-observer variability given the often low spatial resolution, low contrast, dropout, indistinct image boundaries, and other variations and artifacts inherent to ultrasound². Measurement variability can compound e.g. when linear and area measurements are used to calculate volumes and function³. Finally, despite the importance of measurements for all chambers¹, the right heart and left atrium are often neglected in practice, in large part due to the laborious nature of performing additional annotations.

To overcome these problems, researchers have turned to deep learning-based semantic segmentation. To date, supervised approaches have been used for this task^{4–6}, but these require the same manual annotations mentioned above. Therefore, supervised segmentation does not alleviate labeling burden, and instead raises additional concern of using variable and error-prone manual annotations as ground-truth⁷. In fact, to mitigate potential bias from any given human labeler, multiple labelers are advocated, which further increases the cost of labeling⁸. Manual labeling also scales poorly with each additional structure to be labeled, perhaps explaining why most studies of semantic segmentation of the heart to date have focused on the left ventricle^{6,9,10}. In ultrasound, label-free segmentation has proved challenging, despite several attempts^{11,12}. In self-supervised learning (SSL), neural networks are trained with automatically generated labels and human annotation is not required^{13,14}. SSL has been used to segment objects in photographic imaging with some success¹⁵, but to date these approaches are rare in biomedical imaging due to the low acceptable margin of error required for such applications¹⁶.

To bridge the gap between supervised segmentation and the challenges of ultrasound imaging, we hypothesized that weak labels could be created using computer vision techniques, thus circumventing both the time-consuming and subjective nature of human labels. Furthermore, we hypothesized that using these labels in a self-supervised deep learning pipeline designed to mitigate overfitting and incorporate clinical domain knowledge could segment echocardiograms with performance rivaling clinicians, and more robustly than the computer vision techniques alone.

Methods

Methods can be found below in the Supplement.

Results

Overview. After confirming reports^{11,17} that chamber measurements derived from computer vision alone correlate poorly with clinical measures (initial steps in Figure 1 and Supplemental Table 1, Supplemental Figure 2), we developed a pipeline (Figure 1) to provide self-supervised segmentation of echocardiograms. We extracted weak labels for cardiac chambers using traditional computer vision techniques. We then used these weak labels to train more accurate segmentations, utilizing early stopping and clinical domain-guided label refinement in successive neural network training steps to achieve final segmentation performance. The final segmentation predictions were used to calculate standard biometrics for each chamber¹, focusing on the most clinically relevant¹⁸ views: the apical 2-chamber (A2C), apical 4-chamber (A4C), and short-axis mid (SAX). Overall, we used 145,000 images from 450 transthoracic echocardiograms (TTEs) for training and validation, and 4,476,266 images from 8,393 TTEs for testing, each across a range of shapes, sizes, and patient characteristics (Table 1, “all-comers”). A subset of the all-comers (n=553 TTEs) had corresponding cardiac magnetic resonance (CMR) available within 30 days for additional comparison among TTE, CMR, and AI pipeline measurements. Finally, we tested our pipeline against an external dataset of A4C images from 10,030 patients. On the all-comers test set, we achieved Bland-Altman 95% limits of agreement (LOA) between pipeline-derived measurements and clinical echocardiogram measurements similar to human inter- and intra-observer variability^{9,19–21} (Figure 2, Table 3). Determination coefficients (r^2) correlating AI-pipeline-derived and clinical echo measurements ranged from 0.37 for the right ventricular end-systolic area (RVESA), an outlier, to 0.74 for the left ventricular end-systolic volume (LVESV), are consistent with those achieved from supervised deep learning^{5,22}, and are similar to variation encountered clinically (Table 3). For the test subset with corresponding

CMRs, overall correlation between our model and the gold-standard CMR measurements was similar to that of clinical echo measurements and CMR (Figure 2, Figure 3). The pipeline also performed well on external data with a average Dice score of 0.83 (95% CI 0.83).

A pipeline combining computer vision techniques and clinical information with deep learning can segment ultrasound images without the need for human-annotated labels. We used a view classifier²³ to find A2C, A4C, and SAX views and then developed a pipeline for self-supervised segmentation of the cardiac chambers from each view. The pipeline for each view followed the same general steps: initial weak label extraction, early learning correction, chamber edge detection, refinement using aggregate clinical statistical data, and final prediction. The nature and order of these steps differed slightly by view to take advantage of expected chamber shapes and relationships (Figure 1, Supplemental Methods).

For the A2C and SAX views, initial weak labels came from traditional computer vision algorithms—watershed²⁴ and Hough circles²⁵—leveraging known clinical shape priors¹¹ (Figure 1 A1, C1). For the A4C view, initial label extraction utilized the output of the A2C pipeline (Figure 1 B1). The second and third steps of the pipeline were early learning correction and chamber edge detection, applied to the A2C and SAX views. Early learning correction consisted of using early stopping²⁶ to prevent the UNet from learning artifacts or idiosyncrasies of the initial labels (Figure 1 A2, C3). A holistically nested edge detection (HED) network²⁷ was used to strengthen chamber edge detection (Figure 1 A3, C2). (The A4C view did not require these steps because, as above, its initial weak label comes from the A2C prediction where these corrections had already been learned.)

The final step of the pipeline refines the intermediate cardiac chamber predictions using aggregate statistical information about chamber shapes and relationships (Figure 1 A4, B3).

Those refined labels are then fed to a final UNet.

To demonstrate incremental impact of each step of the pipeline on prediction performance and generalizability, labels from intermediate steps of the pipeline were compared to clinical measures on the validation dataset (Supplemental Table 1). For example, r^2 on chamber areas ranged from 0.06-0.22 when using initial weak labels, compared to 0.53-0.81 using the full pipeline. Supplemental Figures 3, 4, and 5 show examples of segmentations from each step for A2C, A4C, and SAX, respectively. These also show that the pipeline can work on high-quality imaging but also on technically difficult or off-axis imaging and across a range of pathologies.

Pipeline-derived structure and function measurements are comparable to clinical echocardiogram measurements. Pipeline-derived measurements in the all-comers dataset were compared to clinical echocardiogram measurements (Figure 2A, Table 2).

Left ventricle. r^2 between the AI pipeline and clinical echocardiogram measurements were 0.65, 0.74, and 0.46 for LVEDV, LVESV, and LVEF in the all-comers test dataset. These correlations are similar to clinician inter- and intra-observer studies^{9,19-21} (Table 3A). Bland-Altman bias \pm LOA for LVEDV, LVESV, and LVEF were $2.2\pm55\text{mL}$, $4.3\pm37\text{mL}$, and $-4.48\pm19\%$, respectively, consistent with those achieved from supervised deep learning^{5,22} (Table 3B).

Right ventricle. Correlation coefficients (r) were 0.74 and 0.53 for RVEDA and RVESA, respectively, indicating a moderate correlation between AI pipeline and clinical echo measurements; r^2 were 0.57 and 0.37 (Table 2).

Atria. The r^2 for left atrial volume was 0.71, showing a good correlation between AI pipeline-derived and clinical echo measurements. Bias \pm LOA was $6.54\pm29\text{mL}$, consistent with inter-

observer bias reported in the literature¹⁹ and also with those reported from supervised learning⁵ (Table 3). Right atrial volume r^2 was 0.6, showing a moderate correlation between clinical echo and AI pipeline-derived measurements (bias \pm LOA 3.78 \pm 31mL; Figure 2, Table 2).

To provide further clinical context, the above measurements and predictions were indexed to body surface area (BSA) where applicable and binned as normal or abnormal according to reference guidelines^{1,28} presented in Figure 3. Pipeline accuracy in predicting normal vs abnormal measurements ranged from 0.71 (LVMI, RVESA) to 0.95 (LVEF) (Figure 3A). These show good accuracy, especially when considering known shortcomings with echocardiography as a clinical gold-standard (Figure 3C).

Self-supervised segmentation correlates to CMR similarly to how clinical echocardiogram compares to CMR. While clinical echo measurements provide the most direct comparison to the AI pipeline-derived measurements, we also compared AI pipeline-derived measurements to CMR where available, since CMR is accepted as the gold standard. Patients in our CMR subset were generally younger, more male, and have more LV dysfunction than all-comers (Table 1). Also, CMRs did not include imaging/measurements for all chambers. Despite these issues, correlations between AI pipeline-derived measurements and clinical echo measurements in this subset was similar to that of all-comers (Table 2).

Comparisons between AI pipeline-derived and CMR measurements of the left ventricle are shown in Table 2 and Figure 2B and 3B. Linear regression analysis gave r^2 between 0.51 and 0.60 for LV size and function, showing a moderate to strong correlation. LV mass was an exception, with $r^2=0.32$; however, it is important to note that the correlation between clinical echo and CMR is also only $r^2=0.27$.

Bland-Altman bias \pm LOA for LVEDV, LVESV, LVEF, and LV mass were -67 ± 115 mL, -28 ± 104 mL, $-8\pm24\%$, and 20 ± 159 g, respectively (Figure 2B). When indexed and binarized into normal vs. abnormal values, accuracies were 0.80, 0.75, 0.84, and 0.61, respectively (Figure 3B). As an internal benchmark, Figure 2C and 3C compare echo measurements and CMR measurements for this same test subset, finding levels of agreement similar to those reported in the literature^{9,29} (Table 3C). Binary normal vs. abnormal accuracies comparing echo and CMR for the left ventricle were 0.83, 0.80, 0.89, and 0.61 for LVEDVI, LVESVI, LVEF, and LVMI (Figure 3C). Taken together, we find that measurements derived from the AI pipeline are about as similar to CMR gold-standard as clinical echo measurements are.

AI pipeline performs well on external data. The external dataset⁶ consisted of 20,060 A4C images from 10,030 patients (one systolic and one diastolic image per patient), with manually annotated clinical tracings of the left ventricle, as well as a computationally-derived LVEF, LVESV, and LVEDV estimation for each patient. As pixel size information was not available, we could not compute dimensional measurements such as, LV height, area, or volume. Instead, performance was measured using Dice score between pipeline-predicted segmentation and the clinical segmentation. While not having many clinical measurements was a disadvantage of this dataset, the ability to compare segmentations between clinician and pipeline on the exact same frame was an advantage. Average Dice score over 20,060 images was 0.83 (95% CI 0.83), representing good agreement (Supplemental Figure 6), especially since errors in clinical labeling or unanticipated views drove some of the low per-image Dice scores (Supplemental Figure 6D-H). With no A2C images available, we estimated LVEF using A4C images alone. When binarized by normal vs. abnormal, accuracy for LVEF was 0.79 compared to estimates provided.

Notably, the AI pipeline predicted segmentations for all four chambers (Supplemental Figure 6), but labels were not available for LA, RV, or RA for performance evaluation.

Discussion

Segmentation is a global, critical, and challenging task in ultrasound—exactly the sort of task that deep learning promises to help with. However, the noisy ultrasound modality presents a conundrum: it is recalcitrant to unsupervised learning, and yet supervised learning would require even more burdensome manual labeling. We solve this conundrum by developing a pipeline for self-supervised¹⁴ segmentation of cardiac chambers from echocardiograms without the need for any manual annotation, to our knowledge the first achievement of its kind.

To demonstrate rigor^{18,30,31}, we tested on large internal and external datasets – over forty times the size of the training dataset. Furthermore, the internal dataset consisted of all-comers with a full range of clinical characteristics and real-world image qualities. Finally, we benchmarked our results against available measurements at several levels: comparing to clinical echo measurements, to CMR, to inter-observer correlations, and to supervised learning.

The scaling implications for self-supervised segmentation in echocardiography are clear. For our training echocardiograms alone, we estimate (based on timed annotations of a small sample) that manually labeling all chambers in all three views would have taken a human 2,496 hours. The fact that both internal and external datasets are missing many segmentations both systematically (e.g. right heart, left atrium) and randomly testify to the laborious nature of segmentation in clinical practice as well. While manual segmentation scales poorly with each additional chamber, our human-labelling-free pipeline can segment all chambers in an image simultaneously. Self-supervised segmentation in ultrasound has the potential to impute segmentations for large datasets, with beat-to-beat and even frame-to-frame granularity as previously demonstrated³², for both clinical and research use. In this manuscript, we focused on measurements we could validate against available clinical measurements from our dataset, but a full range of additional

measurements, such as right atrium ejection fraction (RAEF), left atrium ejection fraction (LAEF), and RV fractional area change (FAC), are immediately possible without additional labor or development required. Scaling to segmentations of other anatomic structures, other views, and other types of ultrasounds are also feasible relatively quickly, using the same building blocks demonstrated in this pipeline.

In achieving self-supervised segmentation for echocardiograms, we demonstrate how traditional computer vision techniques, deep learning, and clinical domain knowledge on chamber shapes and sizes can be combined for medical imaging tasks.

Computer vision choices were driven by the needs of ultrasound imaging, for example, a bilateral filter can remove speckle noise without destroying image features³³. We used two types of neural networks—segmentation networks known to detect ‘textures,’ as well as edge-detection networks to strengthen ultrasound’s noisy boundaries—to obtain better performance than could be obtained from either one alone.

Using a sequence of neural networks in the pipeline (instead of a single neural network going from weak label to final prediction) conferred certain advantages. First, at each training step, we used a handful of weak labels in a self-learning⁴⁸ manner to recruit additional training examples for the next step. Second, we utilized early stopping, since neural networks have been observed learn useful image features early on, before eventually memorizing artifacts and idiosyncrasies^{26,34,35}. In this way, each successive step in the pipeline benefitted from more data with cleaner labels. Note that even extremely weak labels, such as a simple Hough circle for SAX images, resulted in reasonable final segmentation, demonstrating the power of this approach.

We found that using spatial modeling information in our pipeline as clinical domain knowledge improved performance. For example, shape descriptors such as eccentricity and area were used to eliminate segments that cannot exist in real ultrasound exams, and clinical geometric priors were used to stretch the right ventricle to be proportional to the left one.

Study Limitations. Despite promising results, the AI pipeline has also some limitations. While bias \pm LOA from the AI pipeline was comparable to other methods, an ideal pipeline would have even tighter limits of agreement. Changes in the pipeline can further improve segmentation results; in particular, the pipeline may tend to normalize unusual segments (such as Supplemental Figure 5C) and sometimes fails to recognize the endocardial border when it is faint. As future work, we can strengthen and further automate shape information and quality-control rules within the pipeline.

While not a function of the AI pipeline itself, selection of image frames to serve as systolic and diastolic timepoints in real-world ultrasound clips is also a potential source of error (and an open problem affecting supervised segmentation as well⁵).

Additionally, repeated manual measurements on the all-comers dataset from multiple observers could reduce the potential effect of inter-observer measurement error on the clinical ground-truth, but doing this for thousands of echocardiograms was not feasible.

Conclusion. We showed the feasibility of combining Artificial Intelligence (AI) with computer vision techniques and clinical knowledge to automatically generate human-labelling-free chamber segmentations for all four cardiac chambers from ultrasound. This work makes machine learning (ML) for ultrasound efficient and scalable without added work for clinician labelers, relieving a critical bottleneck in ML for ultrasound to date. Furthermore, we demonstrated that the proposed method, tested on more than 18,000 echocardiograms, accomplished a performance

that is comparable to clinical echocardiogram measurements. Overall, it is important to note that the results above were achieved in ultrasound, a clinically essential but highly noisy imaging modality, with zero manually-traced labels. Self-supervised segmentation of ultrasound represents a paradigm shift in how, rather than laboring to provide labels for data-hungry machine learning models, we can get machine learning to work for us efficiently, robustly, and scalably, to solve important problems in cardiology and beyond.

Acknowledgements

We thank the patients, sonographers and physicians whose work created the data used to develop this pipeline.

Contributions

R.A. and D.F. conceived of the study. D.F. performed data analysis with input from R.A. Z.S. performed data acquisition with input from R.A. R.A. and D.F. wrote the manuscript with input from Z.S.

References

1. Lang RM, Badano LP, Mor-Avi V, et al. Recommendations for Cardiac Chamber Quantification by Echocardiography in Adults: An Update from the American Society of Echocardiography and the European Association of Cardiovascular Imaging. *J Am Soc Echocardiogr.* 2015;28(1):1-39.e14. doi:10.1016/j.echo.2014.10.003
2. Thavendiranathan P, Popović ZB, Flamm SD, Dahiya A, Grimm RA, Marwick TH. Improved Interobserver Variability and Accuracy of Echocardiographic Visual Left Ventricular Ejection Fraction Assessment through a Self-Directed Learning Program Using Cardiac Magnetic Resonance Images. *J Am Soc Echocardiogr.* 2013;26(11):1267-1273. doi:10.1016/j.echo.2013.07.017
3. Flachskampf FA, Nihoyannopoulos P. Our obsession with normal values. *Echo Res Pract.* 2018;5(2):R17-R21. doi:10.1530/ERP-17-0082
4. Arnaout R, Curran L, Zhao Y, Levine JC, Chinn E, Moon-Grady AJ. An ensemble of neural networks provides expert-level prenatal detection of complex congenital heart disease. *Nat Med.* 2021;27(5):882-891. doi:10.1038/s41591-021-01342-5
5. Zhang J, Gajjala S, Agrawal P, et al. Fully Automated Echocardiogram Interpretation in Clinical Practice: Feasibility and Diagnostic Accuracy. *Circulation.* 2018;138(16):1623-1635. doi:10.1161/CIRCULATIONAHA.118.034338
6. Ouyang D, He B, Ghorbani A, et al. Video-based AI for beat-to-beat assessment of cardiac function. *Nature.* 2020;580(7802):252-256.
7. Willemink MJ, Koszek WA, Hardell C, et al. Preparing medical imaging data for machine learning. *Radiology.* 2020;295(1):4-15.
8. Irvin J, Rajpurkar P, Ko M, et al. CheXpert: A large chest radiograph dataset with uncertainty labels and expert comparison. In: *Proceedings of the AAAI Conference on Artificial Intelligence.* Vol 33. ; 2019:590-597.
9. Wood PW, Choy JB, Nanda NC, Becher H. Left ventricular ejection fraction and volumes: it depends on the imaging method. *Echocardiography.* 2014;31(1):87-100.
10. Jacobs LD, Salgo IS, Goonewardena S, et al. Rapid online quantification of left ventricular volume from real-time three-dimensional echocardiographic data. *Eur Heart J.* 2006;27(4):460-468. doi:10.1093/eurheartj/ehi666
11. Tavakoli V, Amini AA. A survey of shaped-based registration and segmentation techniques for cardiac images. *Comput Vis Image Underst.* 2013;117(9):966-989.
12. Mazaheri S, Sulaiman PSB, Wirza R, et al. Echocardiography image segmentation: A survey. In: *2013 International Conference on Advanced Computer Science Applications and Technologies.* IEEE;2013:327-332.

13. Ratner A, Bach SH, Ehrenberg H, Fries J, Wu S, Ré C. Snorkel: rapid training data creation with weak supervision. *VLDB J.* 2020;29(2-3):709-730. doi:10.1007/s00778-019-00552-1
14. Jing L, Tian Y. Self-Supervised Visual Feature Learning With Deep Neural Networks: A Survey. *IEEE Trans Pattern Anal Mach Intell.* 2021;43(11):4037-4058. doi:10.1109/TPAMI.2020.2992393
15. Ghosh S, Das N, Das I, Maulik U. Understanding deep learning techniques for image segmentation. *ACM Comput Surv CSUR.* 2019;52(4):1-35.
16. Minaee S, Boykov YY, Porikli F, Plaza AJ, Kehtarnavaz N, Terzopoulos D. Image segmentation using deep learning: A survey. *IEEE Trans Pattern Anal Mach Intell.* Published online 2021.
17. Saini K, Dewal ML, Rohit M. Ultrasound imaging and image segmentation in the area of ultrasound: a review. *Int J Adv Sci Technol.* 2010;24.
18. Kakarmath S, Esteva A, Arnaout R, et al. Best practices for authors of healthcare-related artificial intelligence manuscripts. *NPJ Digit Med.* 2020;3:134. doi:10.1038/s41746-020-00336-w
19. Rodevand O, Bjornerheim R, Ljosland M, Maehle J, Smith HJ, Ihlen H. Left atrial volumes assessed by three- and two-dimensional echocardiography compared to MRI estimates. *Int J Card Imaging.* 1999;15(5):397-410. doi:10.1023/A:1006276513186
20. Keller A, Gopal A, King D. Left and Right Atrial Volume by Freehand Three-dimensional Echocardiography: In Vivo Validation Using Magnetic Resonance Imaging. *Eur J Echocardiogr.* 2000;1(1):55-65. doi:10.1053/euje.2000.0010
21. Mor-Avi V, Sugeng L, Weinert L, et al. Fast Measurement of Left Ventricular Mass With Real-Time Three-Dimensional Echocardiography: Comparison With Magnetic Resonance Imaging. *Circulation.* 2004;110(13):1814-1818. doi:10.1161/01.CIR.0000142670.65971.5F
22. Ghorbani A, Ouyang D, Abid A, et al. Deep learning interpretation of echocardiograms. *NPJ Digit Med.* 2020;3(1):1-10.
23. Madani A, Arnaout R, Mofrad M, Arnaout R. Fast and accurate view classification of echocardiograms using deep learning. *Npj Digit Med.* 2018;1(1):6. doi:10.1038/s41746-017-0013-1
24. Roerdink JB, Meijster A. The watershed transform: Definitions, algorithms and parallelization strategies. *Fundam Informaticae.* 2000;41(1-2):187-228.
25. Yuen HK, Princen J, Illingworth J, Kittler J. Comparative study of Hough transform methods for circle finding. *Image Vis Comput.* 1990;8(1):71-77.
26. Zhang C, Bengio S, Hardt M, Recht B, Vinyals O. Understanding deep learning (still) requires rethinking generalization. *Commun ACM.* 2021;64(3):107-115.

27. Xie S, Tu Z. Holistically-nested edge detection. In: *Proceedings of the IEEE International Conference on Computer Vision.* ; 2015:1395-1403.
28. Petersen SE, Khanji MY, Plein S, Lancellotti P, Bucciarelli-Ducci C. European Association of Cardiovascular Imaging expert consensus paper: a comprehensive review of cardiovascular magnetic resonance normal values of cardiac chamber size and aortic root in adults and recommendations for grading severity. *Eur Heart J - Cardiovasc Imaging.* 2019;20(12):1321-1331. doi:10.1093/ehjci/jez232
29. Dorosz JL, Lezotte DC, Weitzenkamp DA, Allen LA, Salcedo EE. Performance of 3-dimensional echocardiography in measuring left ventricular volumes and ejection fraction: a systematic review and meta-analysis. *J Am Coll Cardiol Img.* 2012;59(20):1799-1808.
30. Sengupta PP, Shrestha S, Berthon B, et al. Proposed Requirements for Cardiovascular Imaging-Related Machine Learning Evaluation (PRIME): A Checklist: Reviewed by the American College of Cardiology Healthcare Innovation Council. *JACC Cardiovasc Imaging.* 2020;13(9):2017-2035. doi:10.1016/j.jcmg.2020.07.015
31. Norgeot B, Quer G, Beaulieu-Jones BK, et al. Minimum information about clinical artificial intelligence modeling: the MI-CLAIM checklist. *Nat Med.* 2020;26(9):1320-1324. doi:10.1038/s41591-020-1041-y
32. Arnaout R, Curran L, Chinn E, Zhao Y, Moon-Grady A. Deep-learning models improve on community-level diagnosis for common congenital heart disease lesions. *ArXiv Prepr ArXiv180906993.* Published online 2018.
33. Shibin Wu, Qingsong Zhu, Yaoqin Xie. Evaluation of various speckle reduction filters on medical ultrasound images. In: *2013 35th Annual International Conference of the IEEE Engineering in Medicine and Biology Society (EMBC).* IEEE; 2013:1148-1151. doi:10.1109/EMBC.2013.6609709
34. Yu S, Chen M, Zhang E, et al. Robustness study of noisy annotation in deep learning based medical image segmentation. *Phys Med Biol.* 2020;65(17):175007. doi:10.1088/1361-6560/ab99e5
35. Liu S, Liu K, Zhu W, Shen Y, Fernandez-Granda C. Adaptive early-learning correction for segmentation from noisy annotations. In: *Proceedings of the IEEE/CVF Conference on Computer Vision and Pattern Recognition.* ; 2022:2606-2616.

Figure Legends

Figure 1. Overview of the segmentation pipeline. (A) A2C segmentation. (A1) Initial weak labels were created by applying a watershed segmentation algorithm to filtered images. (A2) A UNet was trained using the watershed labels (early learning correction and self-learning). (A3) Morphological operations were applied to the output of A2 to create labels to train an edge-detection network. (A4) The output of A3 was then filled in and used to train a second UNet, resulting in a final trained model used for testing. (B) A4C segmentation. (B1) Initial weak labels were created by using the final model from A4 on A4C images, resulting in predictions of two “LA” and two “LV” chambers per image. (B2) Predictions from B1 were reassigned four chamber colors and then used to train a UNet. (B3) A morphological operation was performed on the output of B2 to stretch the RV apex (green dot) to known correlations of RV and LV length (blue box), and then this was used as a label to train a final UNet. (C) SAX segmentation. (C1) Initial weak labels were generated through Hough circle detection. (C2) A HED network was trained using the Hough circles as labels. (C3) The prediction from C2 was then filled in and used as a label to train a second UNet. (C4) Morphological operations were applied to the prediction from C3 to create labels of the epicardial and endocardial areas. A final UNet was trained with these labels on the same images. (D) Clinical calculations. Predictions from A4, B3, and C4 were used to compute chamber dimensions, areas, volumes, and Dice scores on all-comers and external test datasets, respectively. LV = left ventricle (red), LA = left atrium (light blue), RV = right ventricle (dark blue), RA = right atrium (pink), HED = holistically nested edge detection, A2C = apical 2-chamber, A4C = apical 4-chamber, SAX = short-axis mid.

Figure 2. Comparison of clinical and model-derived chamber measurements. Bland-Altman plots comparing (A) AI pipeline-derived measurements vs. clinical echocardiogram

measurements in the all-comers test set and (B) AI pipeline-derived measurements vs. CMR measurements on the subset of test data with corresponding CMRs. As a benchmark, (C) clinical echocardiogram measurements are compared with clinical CMR measurements for this subset. Blue line, mean. Orange shaded lines, 95% limits of agreement. Blue dots represent hearts with normal measurements; orange dots represent hearts with abnormal measurements. LVEDV=LV diastolic volume, LVESV= LV systolic volume, LVEF = LV ejection fraction, RVEDA and RVESA = RV end-diastolic and -systolic areas, respectively.

Figure 3. Comparison of clinical and model-derived chamber measurements binarized into normal vs. abnormal categories. Confusion matrices with accuracy and Cohen's kappa are shown comparing (A) AI pipeline-derived measurements vs. clinical echocardiogram measurements, all-comers and (B) AI pipeline-derived measurements vs. CMR measurements, CMR subset. As a benchmark, (C) Clinical echocardiogram measurements are compared with clinical CMR measurements for that subset. Numbers of echocardiograms shown, with percentage in parentheses. Measurements are indexed by body surface area where clinically applicable. LVEDVI = LV end-diastolic volume index, LVESVI = LV end-systolic volume index, LVEF = LV ejection fraction, LVMI = LV mass index, LAVI = LA volume index, RAVI = RA volume index, RVEDA and RVESA = RV end-diastolic and -systolic areas, respectively.

Tables

Table 1. Demographics and clinical characteristics of the study population for training, validation, and test sets.

	Training &validation set (n=450)	Holdout test set (n=8,393)				TTE vs. Training	TTE vs. TTE-CMR subset	Training vs. TTE vs. TTE-CMR subset	EchoNet external test set (n=10,030)
Characteristics	Nb present	All-comers (n=8,393)		Subset with CMR (n=553)		-	-	-	-
		Nb present	Nb present	Nb present	p-value (mwu)	p-value (mwu)	p-value (kruskal)	-	-
Age, years \pm s.d.(range)	450	58 \pm 17 (20-90)	8393	61 \pm 17 (15-120)	553	50 \pm 16 (19-88)	<0.001	<0.001	<0.001
Female, n (%)	450	220 (49%)	8393	4204 (50%)	553	236 (43%)	0.289	<0.001	<0.001
LV Ejection Fraction <35%, n (%)	402	20 (5%)	5544	468 (6%)	448	72 (16%)	0.210	<0.001	4885 (48%)
LV Ejection Fraction abnormal (qualitative), n (%)	447	89 (20%)	1162	412 (35%)	461	228 (49%)	<0.001	0.259	0.720
LV Diastology abnormal (LVEF), n (%)	333	184 (55%)	798	427 (54%)	316	142 (46%)	0.310	0.015	0.034
LV Size abnormal, n (%)	438	115 (26%)	1125	322 (29%)	444	155 (35%)	0.014	0.010	0.020
LV Mass abnormal, n (%)	381	129 (34%)	983	298 (30%)	363	133 (37%)	0.157	<0.001	<0.001
Measurements									
BSA, m ² , mean \pm s.d.(range)	450	1.88 \pm 0.28 (1.1-2.9)	8393	1.85 \pm 0.26 (0.7-4.3)	553	1.89 \pm 0.25 (1.2-3.1)	0.015	0.031	0.022
LV Ejection Fraction, %, mean \pm s.d.(range)	402	61 \pm 12 (8-83)	5544	60 \pm 12 (4-89)	448	55 \pm 16 (10-86)	0.072	<0.001	<0.001
LV End Diastolic Volume Index, mL/m ² , mean \pm s.d.(range)	402	56 \pm 23 (19-211)	5544	54 \pm 23 (10-244)	448	64 \pm 29 (10-234)	<0.001	<0.001	91.0 \pm 45.7*
LV End Systolic Volume Index, mL/m ² , mean \pm s.d.(range)	402	24 \pm 19 (5-172)	5544	23 \pm 19 (3-203)	448	31 \pm 25 (3-189)	0.020	<0.001	<0.001
LV Mass Index, g/m ² , mean \pm s.d.(range)	335	91 \pm 34 (34-290)	5138	87 \pm 29 (27-293)	391	95 \pm 35 (35-255)	0.002	<0.001	<0.001
LA Volume Index, mL/m ² , mean \pm s.d.(range)	275	31 \pm 14 (10-98)	2177	32 \pm 14 (8-202)	202	33 \pm 14 (9-97)	0.389	0.032	0.144
RA Volume, mL, mean \pm s.d.(range)	-	-	1022	22 \pm 13 (4-143)	-	-	-	-	-
RV End Diastolic Area, cm ² , mean \pm s.d.(range)	-	-	353	17 \pm 5 (7-40)	-	-	-	-	-
RV End Systolic Area, cm ² , mean \pm s.d.(range)	-	-	353	9 \pm 4 (3-28)	-	-	-	-	-

Nb present = number of patients for whom each measurement was available. LV = left ventricle, LA = left atrium, RV = right ventricle, RA = right atrium, BSA = body surface area. mwu = Mann-Whitney U test, two-sided hypothesis. kruskal = Kruskal-Wallis test. Due to size of the datasets, statistical significant differences may be present despite small absolute difference.

Table 2. Comparison of AI pipeline to echocardiographic clinical measurements and CMR.

Test set and comparison		Regression analysis		BA analysis		Number of echos
		r	r ²	Bias	LOA	
LVEDV (mL)						
TTE All-comers	Echo-AI Pipeline	0.74	0.65	2.2 mL	±55 mL	5544
TTE CMR subset	CMR-Echo	0.74	0.66	-59.6 mL	±95.5 mL	448
	CMR-AI Pipeline	0.67	0.53	-67.3 mL	±115.5 mL	448
	Echo-AI Pipeline	0.72	0.63	-7.7 mL	±68.3 mL	448
LVESV (mL)						
TTE All-comers	Echo-AI Pipeline	0.75	0.74	4.3 mL	±37 mL	5544
TTE CMR subset	CMR-Echo	0.76	0.74	-35 mL	±84.5 mL	448
	CMR-AI Pipeline	0.71	0.6	-27.5 mL	±104.4 mL	448
	Echo-AI Pipeline	0.78	0.69	7.6 mL	±51.4 mL	448
LVEF (%)						
TTE All-comers	Echo-AI Pipeline	0.56	0.46	-4.48 %	±19 %	5544
TTE CMR subset	CMR-Echo	0.76	0.68	3.33 %	±19.8 %	448
	CMR-AI Pipeline	0.71	0.51	-8.24 %	±24.3 %	448
	Echo-AI Pipeline	0.72	0.54	-11.57 %	±21.5 %	448
LV mass (g)						
TTE All-comers	Echo-AI Pipeline	0.71	0.56	13.4 g	±74.1 g	5138
TTE CMR subset	CMR-Echo	0.68	0.27	11.2 g	±166.5 g	49
	CMR-AI Pipeline	0.66	0.32	19.9 g	±158.5 g	49
	Echo-AI Pipeline	0.78	0.67	8.7 g	±76.5 g	49
LA volume (mL)						
TTE All-comers	Echo-AI Pipeline	0.78	0.71	6.5 mL	±29 mL	2177
RA volume (mL)						
TTE All-comers	Echo-AI Pipeline	0.69	0.6	3.8 mL	±31.4 mL	973
RVEDA (cm²)						
TTE All-comers	Echo-AI Pipeline	0.74	0.57	4.0 cm ²	±7.0 cm ²	353
RVESA (cm²)						
TTE All-comers	Echo-AI Pipeline	0.53	0.37	2.5 cm ²	±8.0 cm ²	353

LVEF = left ventricular ejection fraction, LVEDV = left ventricular end-diastolic volume, LVESV = left ventricle end-systolic volume, RVEDA = right ventricular end-diastolic area, RVESA = right ventricular end-systolic area, r = Spearman correlation coefficient, BA = Bland-Altman, LOA = 95% limits of agreement, TTE = transthoracic echocardiogram, CMR = cardiac MRI.

Table 3. Comparison of AI pipeline performance to literature.

Evaluation method	Number of images/patients training set	Reference	Statistic	LVEDV (Nb test)	LVESV (Nb test)	LVEF (Nb test)	LV mass (Nb test)	LA volume (Nb test)
(A) Echocardiogram inter-observer variability	N/A	Rodevand et. al. ¹⁹	bias±LOA	N/A	N/A	N/A	N/A	4% to 16%, ±45% to ±55% *† (18)
	N/A	Mor-Avi et. al. ²¹	bias±LOA	N/A	N/A	N/A	37±19%* (50)	N/A
	N/A	Jacobs et. al. ¹⁰	bias±LOA	23±42 (50)	11±20 (50)	8±18 (50)	N/A	N/A
	N/A	Keller et. al. ²⁰	bias±LOA	N/A	N/A	N/A	N/A	N/A±22.3mL (25)
	145k/450	AI pipeline	bias±LOA	2±53mL (5544)	4±35mL (5544)	-4±19% (5544)	10±35% * (5138)	6±29mL or 11±49% * (2177)
(B) Supervised neural network	172k/2,546 ‡	Ghorbani et. al. ²²	bias±LOA	N/A±58 mL (337)	N/A±41mL (337)	N/A±21% (337)	N/A	N/A
			r2	0.7	0.74	0.5	N/A	N/A
	526/277	Zhang et. al. ⁵	bias±LOA	2±56mL (8457)	N/A±39 mL (8427)	-5±20% (6407)	N/A±91g (5952)	5±33mL (4800)
	145k/450	AI pipeline	bias±LOA	2±53mL (5544)	4±35mL (5544)	-4±19% (5544)	13±74g (5138)	6±29mL (2177)
			r2	0.65	0.74	0.46	N/A	N/A
(C) CMR-echo	N/A	Wood et. al. ⁹	bias,±LOA	-140mL to - 20mL, ±30mL to ±130mL † (up to 1087)	-100mL to - 5mL, ±25mL to ±120mL (up to 1087)	-5% to 10%, ±10% to ±22% † (up to 1087)	N/A	N/A
	145k/450	AI pipeline	bias±LOA	-67±115 mL (5544)	-27±104 mL (5544)	-8±21% (5544)	N/A	N/A

* computed as the percentage difference between observers/methods.

† displayed as a range of values reported by the many approaches discussed in the cited paper, i.e. the lower and upper limits for each metric mentioned.

‡ labels are numerical values extracted from clinical reports and not manual annotation.

Nb = numbers.

Figures

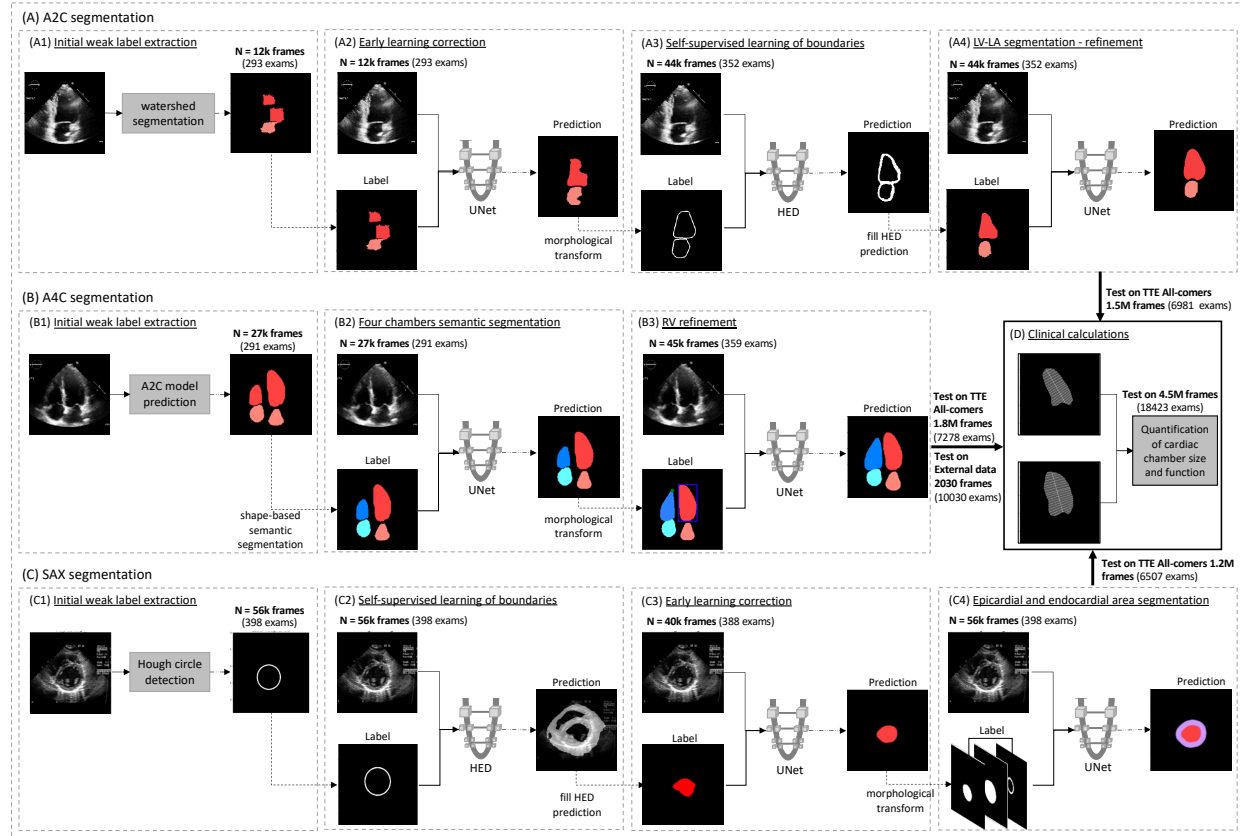


Figure 1. Overview of the segmentation pipeline.

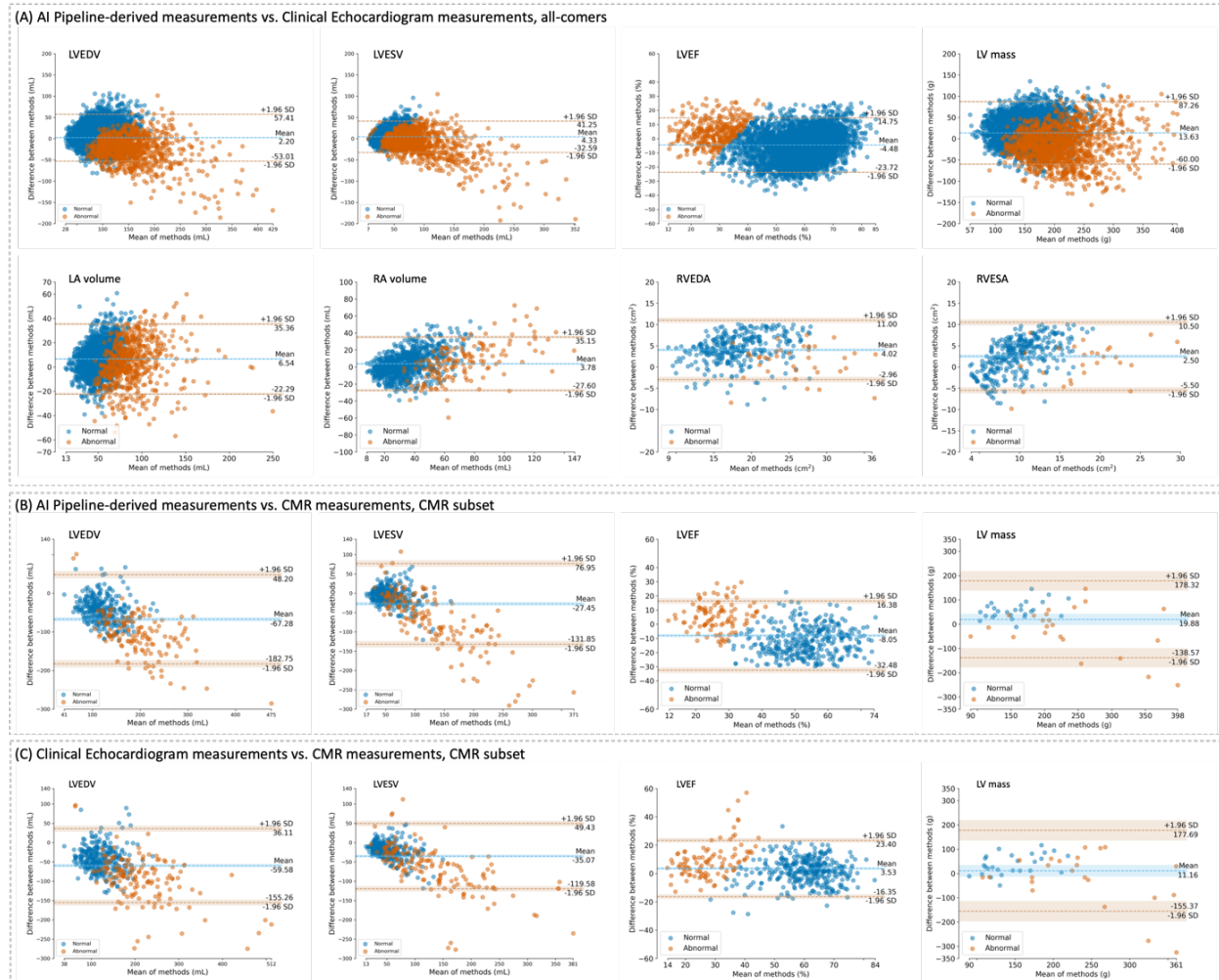
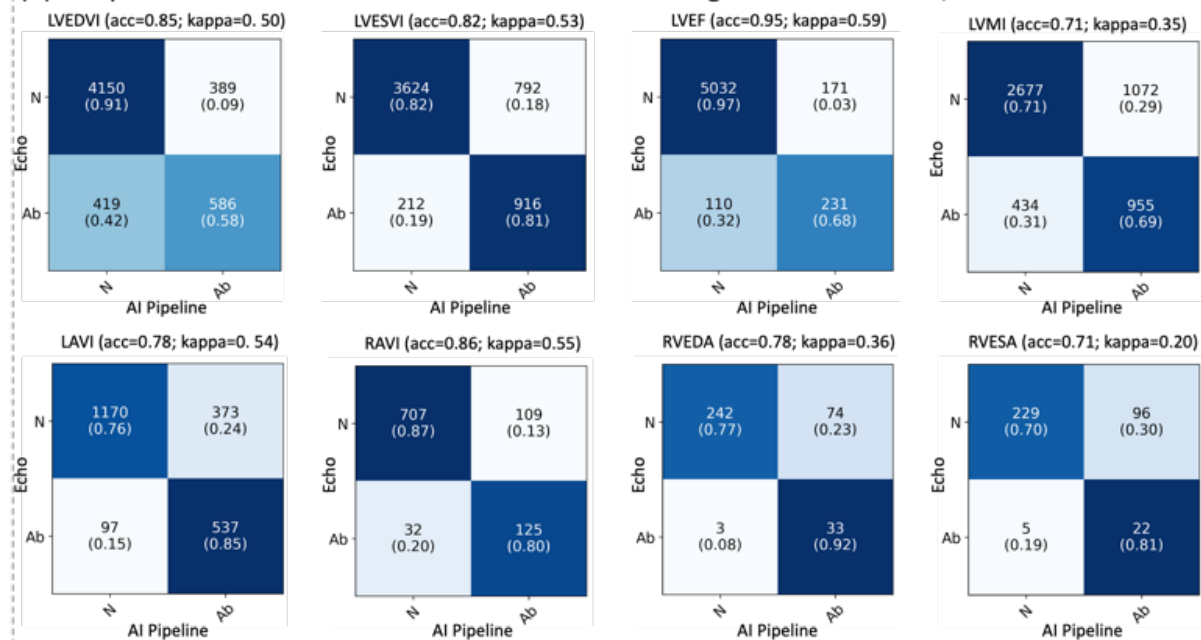
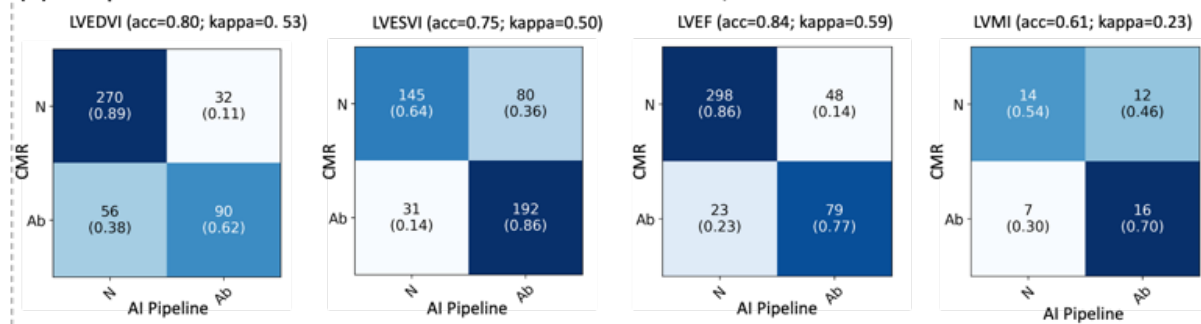


Figure 2. Comparison of clinical and model-derived chamber measurements.

(A) AI Pipeline-derived measurements vs. Clinical Echocardiogram measurements, all-comers



(B) AI Pipeline-derived measurements vs. CMR measurements, CMR subset



(C) Clinical Echocardiogram measurements vs. CMR measurements, CMR subset

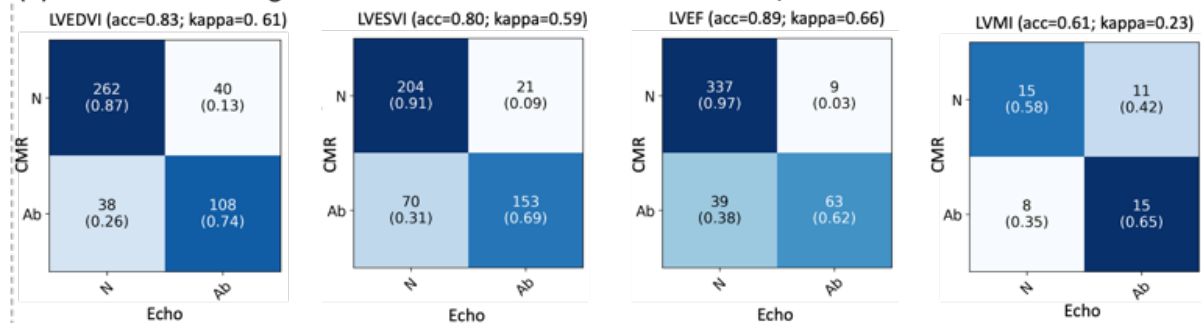


Figure 3. Comparison of clinical and model-derived chamber measurements binarized into normal vs. abnormal categories.

Supplement

Supplemental Methods

Datasets. *Internal dataset.* A total of 8,843 unique deidentified patient echocardiograms from UCSF were used (Table 1), with waived consent in compliance with the Institutional Review Board at the UCSF. All clinically interpretable studies were included regardless of image quality. apical 2-chamber (A2C), apical 2-chamber (A4C) and short-axis mid (SAX) b-mode views were identified as previously described¹. Views with color Doppler or LV contrast were excluded. For training and validation datasets, only images with a 200mm field of view (FoV) were included. Estimated heart rate was computed using DICOM metadata, and only images from the first heart cycle were used to reduce image-level redundancy².

Training and validation subset. 450 echocardiograms (1,935 videos and 145,000 images) divided over 3 separate views (i.e., A2C, A4C, and SAX) were used to develop the AI pipeline. Up to eighty percent (up to 360 echocardiograms) were used for training, and 20% (90) for validation at each step of the pipeline. *Test subset.* 8,393 echocardiograms (4,476,266 images) were used as a holdout test set. A subgroup of the holdout set also had cardiac magnetic resonance (CMR) exams, performed \pm 30 days from the date of the corresponding echo (n=553 echos, “CMR test subset”). Measurements, such as left ventricle (LV) ejection fraction (LVEF), LV end-diastolic volume (LVEDV), LV end-systolic volume (LVESV), LV mass index (LMI), left atrial (LA) volume, right atrial (RA) volume, and right ventricular (RV) end-diastolic area (RVEDA) were extracted from the echocardiogram database and used as ground-truth labels for performance evaluation for all test echocardiograms. Where indicated in the Results, these measurements were indexed by body surface area. Additionally, for the CMR test subset, corresponding measurements were extracted from the clinical CMR reports. To evaluate test performance for a given chamber, only studies with available clinical measurements were used. A flow diagram

showing this is in Supplemental Figure 1. Training, validation, and test sets did not overlap by image, patient, or study.

External dataset. An external test dataset was obtained from

(<https://echonet.github.io/dynamic/>).

Data preprocessing. The ultrasound region of interest was extracted from DICOM images and normalized to a size of 0.5mm/pixel. The resulting images were resized (using area interpolation) to 256x256 pixels for segmentation networks or to 480x480 pixels for edge detection networks. Pixel intensities were normalized from 0 to 1. Areas outside the ultrasound region were masked. Preprocessing steps made use of open-source Python 3.6 libraries OpenCV v4.4(<https://opencv.org/>), scikit-image (<https://scikit-image.org/>) and NumPy v1.20 (<https://numpy.org>).

Neural network architectures. *Segmentation network.* A UNet was used for segmentation tasks as described³ except for the following modifications: the 1x1 output layer was sigmoid-activated, Adam optimizer was set with a learning rate of 1e-4, loss function was soft dice loss and batch size was 32. Data augmentation to improve model training consisted of random image modifications to ~20 percent of training data as follows: rotations from 0-10 degrees, width and height shifts from -10% to +10%, zoom from -20% up to +20%, shear factor from 0 to 0.03, horizontal flips, contrast stretching between 2nd and 98th percentile of pixel intensity values, and cropping of 160x160 pixel patches.

Edge-detection network. A holistically nested edge detection (HED) network was implemented for edge-detection tasks as described⁴ except for the following modifications: the model was initialized with ImageNet weights and fine-tuned using the same hyperparameters as in Xie et al

⁴ with a batch size 8. The following data augmentations were randomly applied: rotations 0-10 degrees, width and height shifts $\pm 10\%$, zoom $\pm 8\%$, shear factor 0-0.03, and horizontal flips. All models were implemented in Keras 2.2.4 (<https://keras.io/>, GitHub, 2015) and a TensorFlow 1.15.2 (<https://www.tensorflow.org/>) backend and trained in a NVIDIA Tesla M60 GPU with 8GiB of memory.

Early learning correction during network training. Deep neural networks have been observed to be robust to label noise and first fit the training data with clean labels during the early learning phase, before eventually memorizing the examples with false labels ⁵⁻⁹. Aligned with these findings, we exploited early learning in training the segmentation networks used in this study. During network training, the soft dice loss curve for the validation dataset was monitored in TensorBoard 2.3.0 (www.tensorflow.org). The transition from the transient phase (early learning) to the memorization phase was detected where the bend of the soft dice loss curve in a shape of elbow is observed i.e., where the slope of the curve changes. Training was stopped at the elbow point (early stopping), thus avoiding the network of correcting small mistakes in the label.

Self-learning during network training. In several neural network training steps, a neural network trained on a portion of training data with available weak labels was then used to infer on *all* available training and validation data in a self-learning manner¹⁰, to recruit additional labeled training examples. This is further detailed below.

Clinical calculations. The output of the segmentation model was used to compute chamber dimensions, i.e., areas and volumes, for A2C, A4C and SAX views according to clinical guidelines¹¹. For each metric, we inferred the segmentation model in all frames of all videos that included the chamber of interest. Lengths and areas were calculated based on a squared-pixel

size of 0.5mm. For determining systole vs diastole frames, for each chamber of interest, segmentations were plotted by frame and max and min areas were identified¹² for all videos. The frame with the largest area over all videos was selected to be diastole, and smallest frame of the same video to be systole. LV and LA volumes were calculated from A2C and A4C views, using the biplane method of disks summation (modified Simpson's rule)¹¹, LV mass from SAX and the largest LV length between A2C and A4C views¹¹. RA volume and RV area were computed from A4C view using disks summation technique. LVEF was calculated using the formula¹¹, $LVEDV - LVESV / LVEDV$. LV mass calculation used the area-length method¹¹, and was calculated using the following formula: $1.05 \{ [5/6 A1(a+d+t)] - [5/6 A2(a+d)] \}$, where A1 is the epicardial cross-sectional area, A2 the endocardial cross-sectional area, a is the distance from the minor axis to the mitral valve plane, d the distance from the minor axis to the mitral valve plane, and t is the mean wall thickness.

Statistical Analysis. Spearman rank correlation was used to measure the linear relationship between CMR, echocardiography and AI pipeline-derived chamber measurements. Linear regression analyses were performed to measure the strength of their relationships. Differences between distributions of measurements were tested using the nonparametric Mann Whitney U (mwu) test; a p-value <0.05 was considered statistically significant, although due to dataset size, even minimal differences were often found to be statistically significant. Bland-Altman (BA) plots were analyzed to demonstrate the bias and limits of agreement between different methods for each measurement. Cohen's Kappa was used to assess the agreement between the normal and abnormal values determined by different methods. All statistical testing was performed using the scipy package (<https://pypi.org/project/scipy/>) in Python 3.

Code Availability. Code will be made available upon publication at github.com/ArnaoutLabUCSF/CardioML

A2C Segmentation. *A1. Initial weak label extraction.* A bilateral filter¹³ (geometric closeness $\sigma_s = 15$, photometric similarity $\sigma_r = 0.25$), using scikit-image (<https://scikit-image.org/>), was applied to echo images for speckle noise reduction¹³. An Euclidean distance transform (minimum distance = 20 pixels) was applied to the bilateral-filtered image to propose seed points for the watershed algorithm using scipy.ndimage (<https://pypi.org/project/scipy/>). The watershed algorithm¹⁴ (scikit-image) was applied to create segments according to the seed points. At this point, ideally there are only two watershed segments each corresponding to a cardiac chamber, but there may be more or fewer than two, and some may stray outside the blood pool region. A copy of the bilateral-filtered image was binarized (threshold = 0.1) and regions smaller than 500 pixels and holes with area smaller than 1000 pixels were removed, to create a mask for the blood pool. This mask was applied to the watershed image to remove segments outside the blood pool area. Next, a topological descriptor was used—the number of connected components in the image—to exclude images where the watershed algorithm was not able to find at least two segments. Then, the centroid of each watershed segment was computed and any not belonging to the region of interest (the blood pool) were eliminated. The remaining suitable segments were labeled as ‘LA’ or ‘LV’ according to the known spatial relationship of these chambers in the A2C view. Finally, as a post-processing step, we employed shape descriptors such as eccentricity and area to eliminate chamber segments that cannot exist in real ultrasound exams (these may represent partial chambers from a zoomed-in image, or segments that are erroneously large). Cutoffs for area were 6 to 75cm² and 4.7 to 104cm², and eccentricity between 0.16 to 0.94 and 0.35 to 0.97 for left atrium and left ventricle, respectively.

A2. Early learning correction of noisy labels and self-learning. Initial weak labels were used to train a UNet on 12,000 images (n=293 echos), split 80/20 (train/val) patient-wise, for 5 epochs, using early stopping as discussed above. It is important to note that while step A1 resulted in thousands of images with suitable weak labels for training step A2, it also failed on many of those images that remained unlabeled (see “Initial weak label extraction” above, where images/labels would be discarded if labels didn’t meet various thresholds or criteria). To recruit additional usable labels from the training images that the initial weak label method was not able to adequately segment, we used self-learning¹⁰. Namely, at every pipeline step after A1 (Figure 1), inference from that step was run on all training and validation data to generate additional weak labels and to increase the accuracy of the initial weak labels for the subsequent steps, namely steps A3, A4, B3, C3, and C4 of the pipeline. For example, the UNet trained in step A2 was used to infer on all the training and validation images, including the ones that had failed step A1, creating more usable labels step A3. (Test data was always held completely separate from this process.)

A3. Self-supervised learning of boundaries. Labels for training the HED model were created by applying morphological operations (dilation-erosion) to the convex hull of UNet predictions from step A2. The HED network was trained using 44,000 frames from 352 unique patients for 15 epochs utilizing early stopping described above. Morphological operations were performed using scikit-image (<https://scikit-image.org/>).

A4. Segmentation Refinement. Labels for training step A4 were created from the predictions from step A3 as follows. Step A3 predictions were filled in using the binary_fill_holes function of scipy.ndimage package. LA and LV were assigned as in step A1. Quality control was provided by shape descriptor analysis, discarding chambers of unreasonable size/eccentricity as in A1;

additionally, LV contours with height/width ratio less than 2 were stretched by a given factor α ($\alpha = 2/\text{height}$), when the length of the LV was not proportional to the base size of the LV. A UNet was then trained using the resulting labels to provide a refined segmentation, utilizing early stopping as described above. The UNet was trained in 44,000 frames of 352 unique patients for 7 epochs.

A4C Segmentation. *B1. Initial weak label extraction.* Initial weak labels for step B1 were created as follows. The trained UNet from step A4 was used to predict segmentations for A4C images (resulting in predictions with two LAs and two LVs per image). Centroids were calculated for each segment and spatial relationships leveraged to re-label these chambers as RA, RV, LA, and LV (as in A1). Shape and topological descriptors were used to discard images whose segmentations failed size and eccentricity thresholds, and which lacked four connected components (as in A1); acceptable areas were 6-75 cm² for LA and RA, 4.7-104 cm² for LV and RV; acceptable eccentricities were 0.3-0.96 for LA, 0.17-0.95 for RA, 0.62-0.96 for LV, and 0.65-0.96 for RV.

B2. Four chamber semantic segmentation. Labels from B1 were used to train a UNet for noise reduction and semantic segmentation of the four chambers. The network was trained on 27,000 frames from 291 unique patients split 80/20 (train/val) patient-wise for 5 epochs. To assist in learning a better model, similarly to A2, this model was used to infer on the training and validation images in a self-learning approach to generate additional weak-label and to increase the accuracy of the initial-weak-label for B3, resulting in 45,000 frames from 359 echos.

B3. Right ventricle refinement. Predictions from B2 were noted to have systematically shorter RV length than appropriate. Labels for B3 were therefore created from the predictions from B2, refining them based on spatial priors as follows. Length of the predicted LV and RV segments

were measured, and its ratio β (RV height/LV height) computed. If the ratio β was less than 0.8, that is RV height was 80% of the LV height value or smaller, the RV segment was stretched to be proportional to the LV. Specifically, a bounding box was drawn around the predicted LV segment and the length of the bounding box was calculated; the RV segment was then stretched so that its length was the same as that of the LV bounding box. Using the resulting labels, the UNet resulting in a final prediction for A4C segmentations. The network was trained on 45,000 frames of 359 unique patients for 5 epochs. All measurements made use of measure package of scikit-image (<https://scikit-image.org/>).

SAX segmentation. *C1. Initial weak label extraction.* In the SAX view, the LV has a donut shape as a clinical prior. The Hough circle transform¹⁵ was therefore used to create the initial weak label. First, a median blur filter (kernel size = 9) was applied to images to reduce noise. Then, a Laplacian operator (kernel size = 5) was employed to extract edges and to reduce the amount of data in the image, an important step to reduce the computation time of the Hough transform. Finally, the Hough transform was applied to detect the center and the radius of the endocardial region. Parameters for the Hough transform were a minimum distance between the centers of the detected circles of 400, minimum and maximum circle radius of 20 and 80, respectively. All image processing made using the OpenCV library.

C2. Self-supervised learning of boundaries. The circle drawn from the Hough transform output was used as a label to train a HED network using early stopping as above. The network was trained with a dataset of 56,000 frames from 398 unique patients, split 80/20 (train/val) patient-wise, for 20 epochs. Self-learning was then used to infer on the training and validation sets to produce weak labels for C3, resulting in 40,000 frames from 388 echos. Note that this number of images is smaller than the number of initial labels used to train the HED network. This was

because there were no failures to generate a Hough circle (although the size or location of the Hough circles may still be inaccurate). On the other hand, if the image is too noisy, the HED may not be able to identify the LV lumen and the inference would fail.

C3. Early learning correction of noisy labels. To correct the noisy labels generated by the HED outputs we used the same method as described in Step A3. The HED predictions from C2 were filled in to create weak labels of the LV lumen. These resulting labels were then used to train a UNet to correct noisy labels on the same initial dataset (using early stopping). The network was trained with a dataset of 40,000 frames of 388 unique patients for 5 epochs. Self-learning was then used to infer on the training and validation set to generate more data and to refine the weak labels for C4, resulting in 56,000 frames from 398 echos.

C4. Epicardial and Endocardial segmentation. The predictions from C3 (LV lumen area only) were used to create labels for C4 (LV lumen and myocardium) as follows. A myocardial label was created by dilating (randomly ranging between 6-14 pixel thickness) and eroding (randomly ranging between 3 and 6 pixels) the LV lumen shape to create a myocardial rind around the LV lumen. The resulting labels (now consisting of LV lumen, LV myocardium, and background) were used to train a UNet for a round of noise label correction using the same 56,000 images from 398 echos from C3 for 5 epochs.

Supplemental Table 1. Comparison of echocardiography clinical measurements to model prediction from successive pipeline steps in the validation dataset.

Clinical measurement	Pipeline step (Fig. 1)	Regression analysis		Bland-Altman analysis		Nb patients
		r	r ²	Bias (cm ²)	LOA (cm ²)	
LV area, A2C (diastole)	(A1)	0.28	0.1	-6.35	37.97	60
	(A2)	0.76	0.51	-1.23	28.39	66
	(A3)	0.71	0.41	-4.72	25.75	66
	(A4)	0.77	0.57	3.83	26.26	66
LV area, A2C (systole)	(A1)	0.43	0.18	0.46	24.44	60
	(A2)	0.64	0.5	-0.33	22.46	66
	(A3)	0.74	0.56	-0.38	19	66
	(A4)	0.75	0.68	1.6	17.08	66
LA area, A2C	(A1)	0.39	0.22	-1.38	20.05	60
	(A2)	0.73	0.72	-0.83	15.88	66
	(A3)	0.76	0.68	-3.55	13.84	66
	(A4)	0.78	0.81	0.23	11.21	66
LV epicardial area, SAX	(C1)	0.25	0.06	-13	26	80
	(C2)	0.49	0.25	7.58	32.66	80
	(C3)	0.52	0.39	0.43	19.68	83
	(C4)	0.55	0.53	2.34	18.85	83
LV endocardial area, SAX	(C4)	0.55	0.6	-0.05	30	83

A2C = apical 2-chamber view. SAX = short-axis mid view. LV = Left ventricle. LA = Left atrium. r = Spearman correlation coefficient. LOA = limit of agreement. Nb= total number of patients in the validation dataset with the clinical measure of interest present.

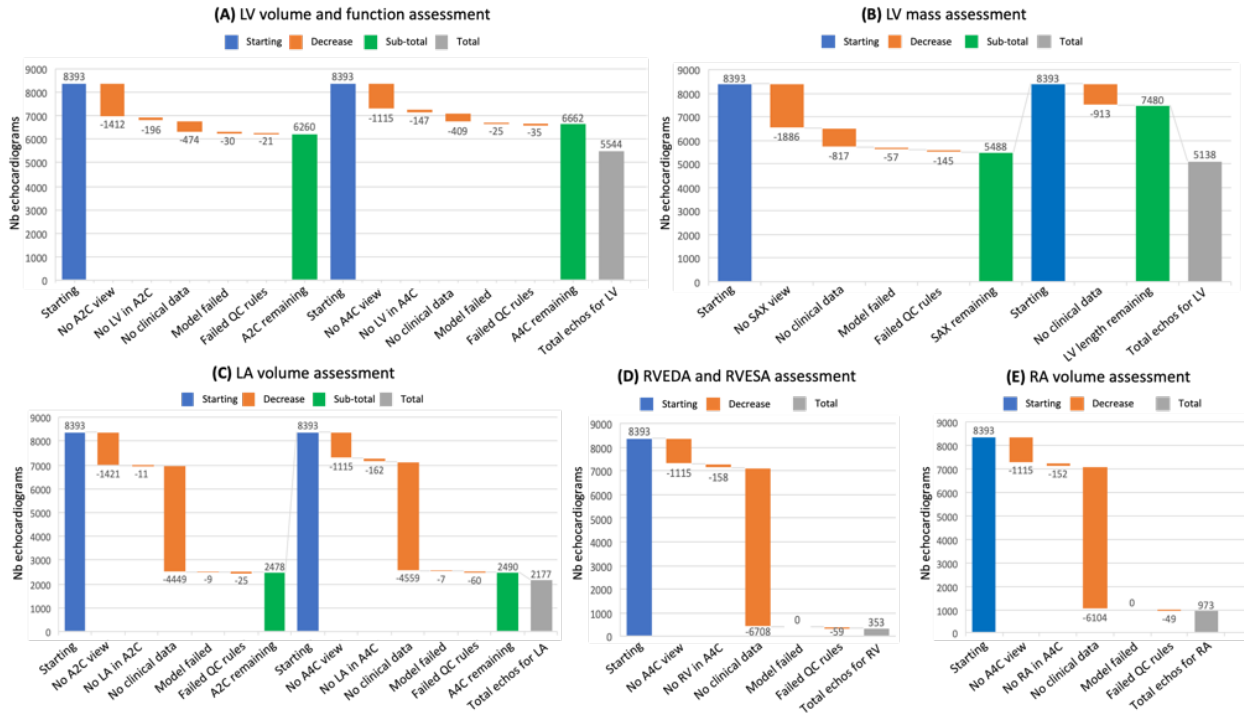
Supplemental Table 2. Model performance of LV segmentation in an external dataset.

Dataset	EchoNet dataset (Nb patients)	Average Dice Score, Diastole [95% CI*]	Average Dice Score, Systole [95% CI*]
EchoNet model [†]	EchoNet test set (1,277)	0.927 [0.925 - 0.928]	0.903 [0.901 - 0.906]
Our model	EchoNet test set (1,277)	0.858 [0.854 - 0.862]	0.807 [0.80 - 0.813]
	Whole dataset (10,030)	0.855 [0.854 - 0.857]	0.81 [0.808 - 0.812]

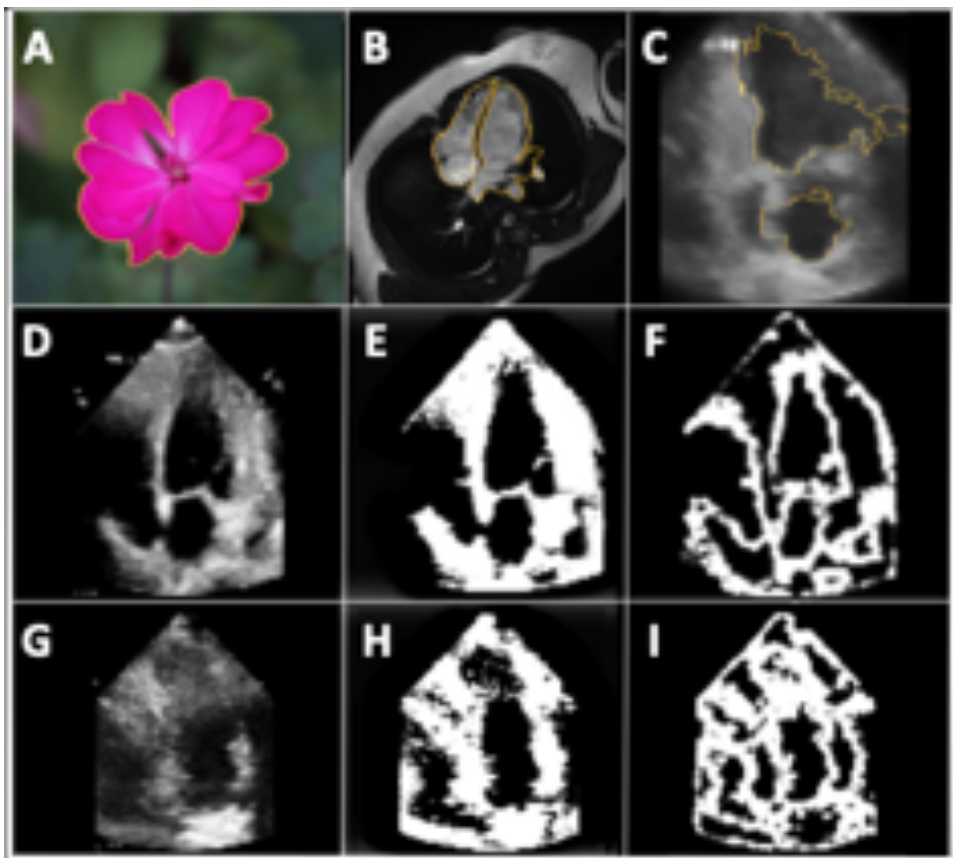
Nb = number

* Confidence intervals were computed using 10,000 bootstrapped samples

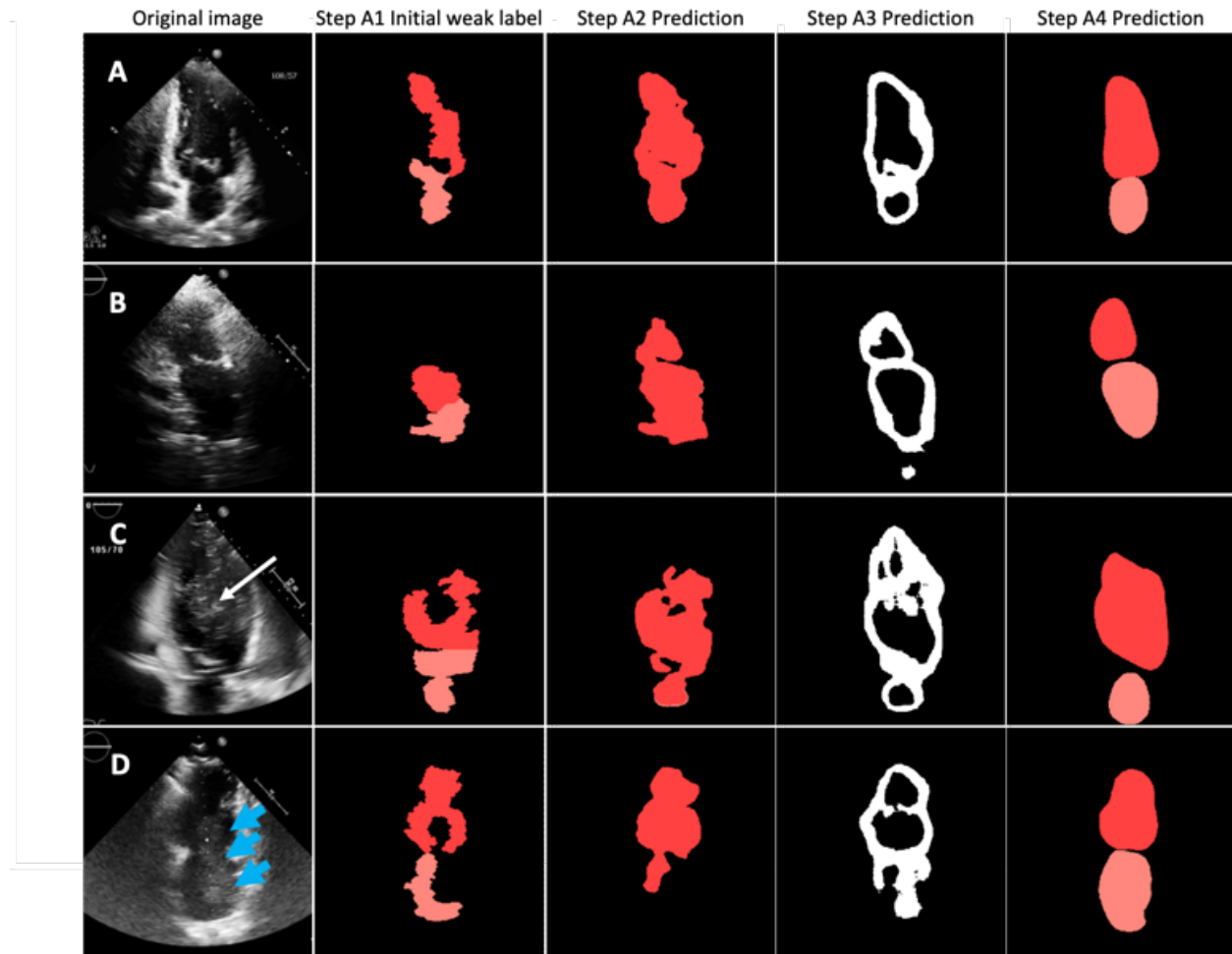
† Values for EchoNet test set were extracted directly from the paper¹⁶ since the EchoNet model is not available.



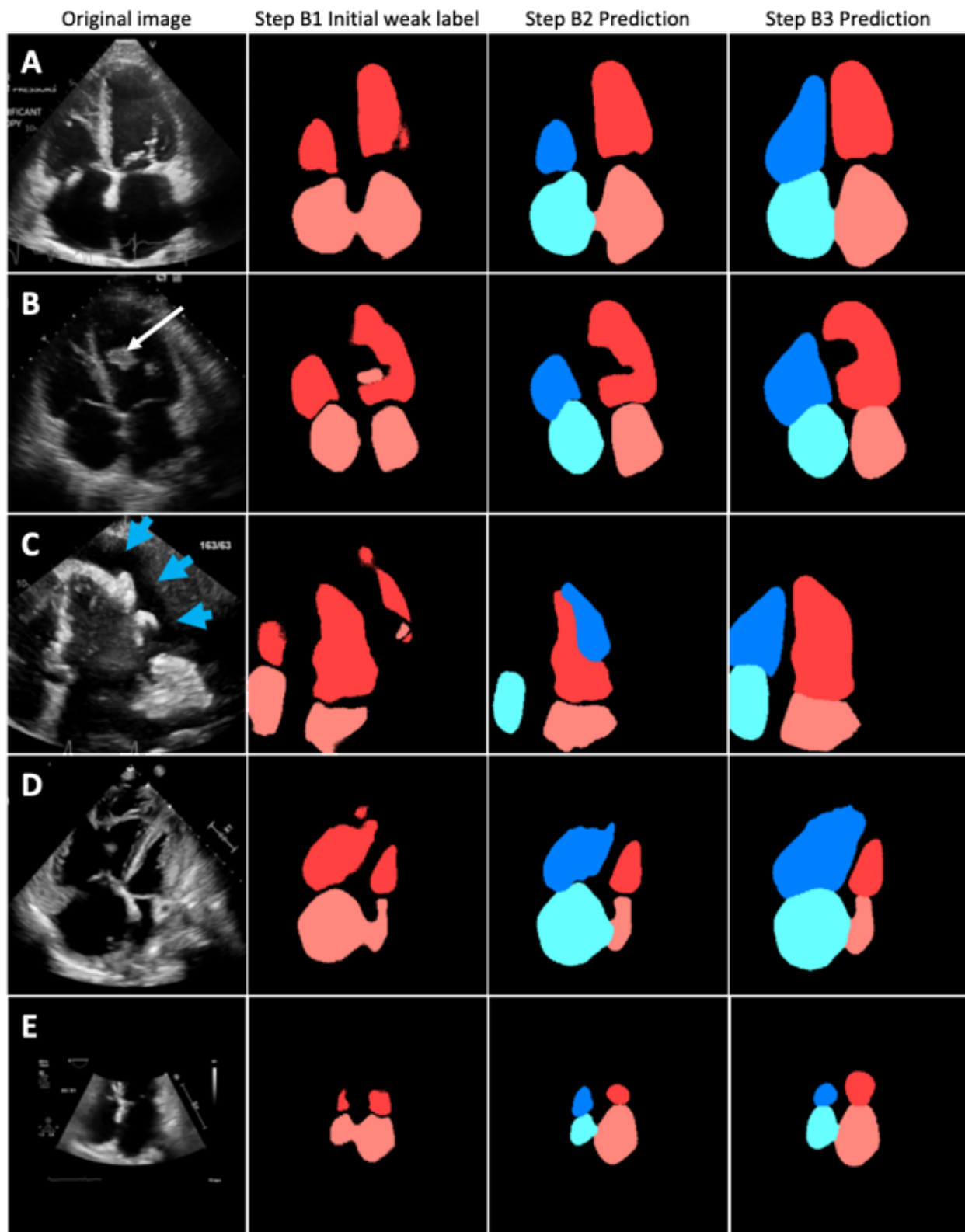
Supplemental Figure 1. Inclusion/exclusion of test data by clinical measurement. The test set had 8,393 echocardiograms/patients. For each measurement assessed, certain views and chambers needed to be present in the echocardiogram as above; a clinical measurement needed to be present in the echocardiogram report for ground-truth comparison. (A) shows the echocardiograms containing A2C and A4C views and clinical ground-truth measurements of the LV for LV size and function assessments. (B) shows the echocardiograms containing SAX views of the LV and LV length measurement for LV mass assessment. (C) shows the echocardiograms containing A2C and A4C views/measurements of the LA, while (D) and (E) show the A4C views/measurements needed for RV and RA assessment, respectively. LV = left ventricle, LA = left atrium, RV = right ventricle, RA = right atrium, QC = quality control, A2C = apical 2-chamber view, A4C = apical 4-chamber view, SAX = short-axis mid view, Nb = number. “No clinical data” = no clinical echocardiogram measurement for comparison to ground truth, “Model failed” = model did not predict anything, “Failed QC rules” = model predicted a chamber, but its shape and/or size failed post-processing rules.



Supplemental Figure 2. Examples of standard computer vision methods on different images. First row – classical computer vision watershed algorithm (thin yellow line) applied to (A) a photo image of a flower, and medical images of the heart in (B) MRI and (C) ultrasound modalities. Note that this algorithm works best on a photo image. Second and third rows depict two echo image examples – left (D,G): original echo images, middle (E,H): segmentation using bilateral filtering, right (F,I): segmentation using optical flow between consecutive frames of the echocardiography sequence.

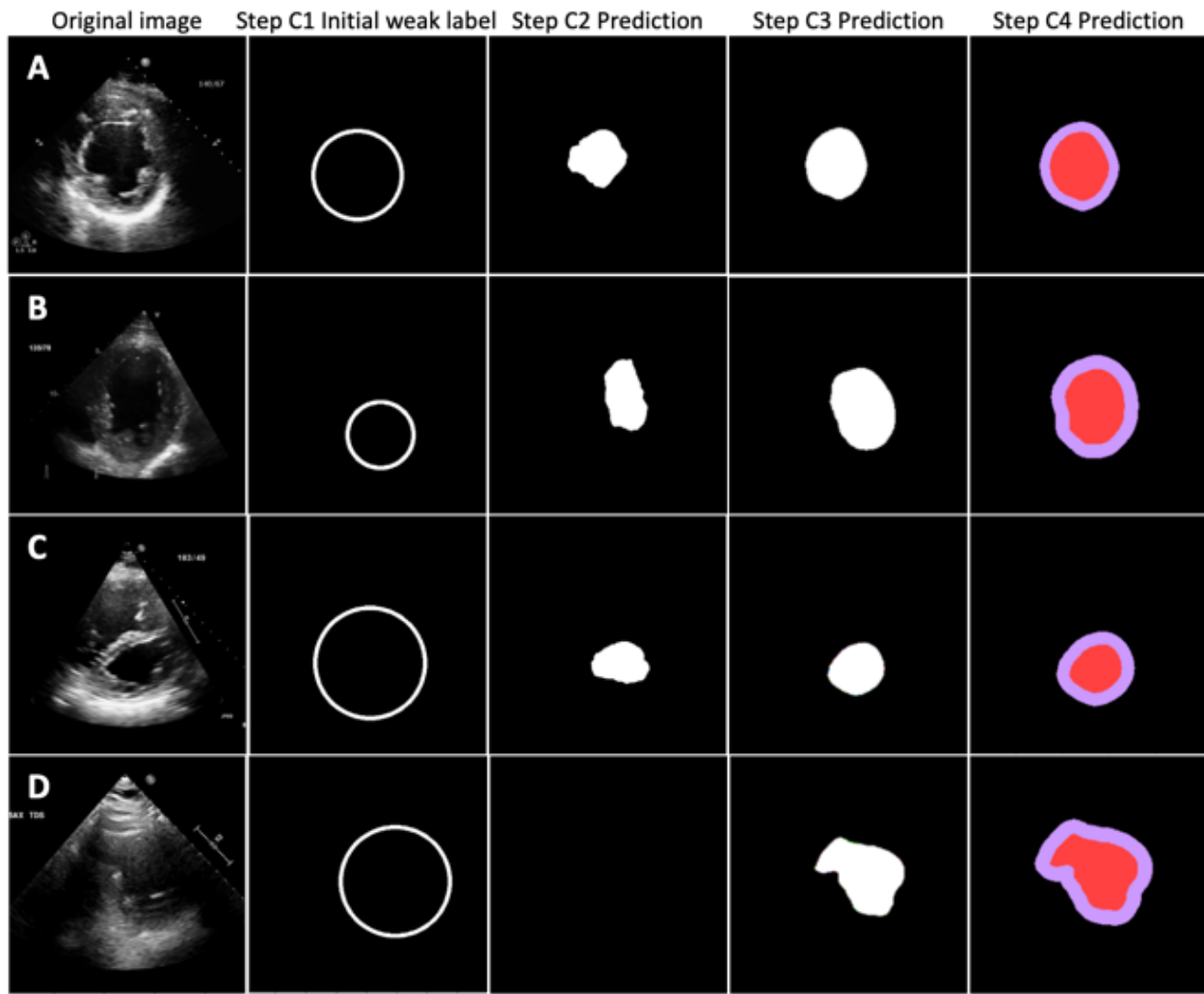


Supplemental Figure 3. Examples of A2C images at each step of the AI pipeline. (A) shows a typical good-quality A2C image: the initial weak label (step A1) segment the chambers poorly, but are corrected through successive steps of the pipeline to final prediction (step A4). The pipeline performs well even with left atrial enlargement in a technically difficult image (B), an image where LV contrast (white arrow) obscures the LV lumen (C), and an image with a large LA mass (blue arrowheads) prolapses into the LV (D). A2C = apical 2-chamber, LV = left ventricle, LA = left atrium.

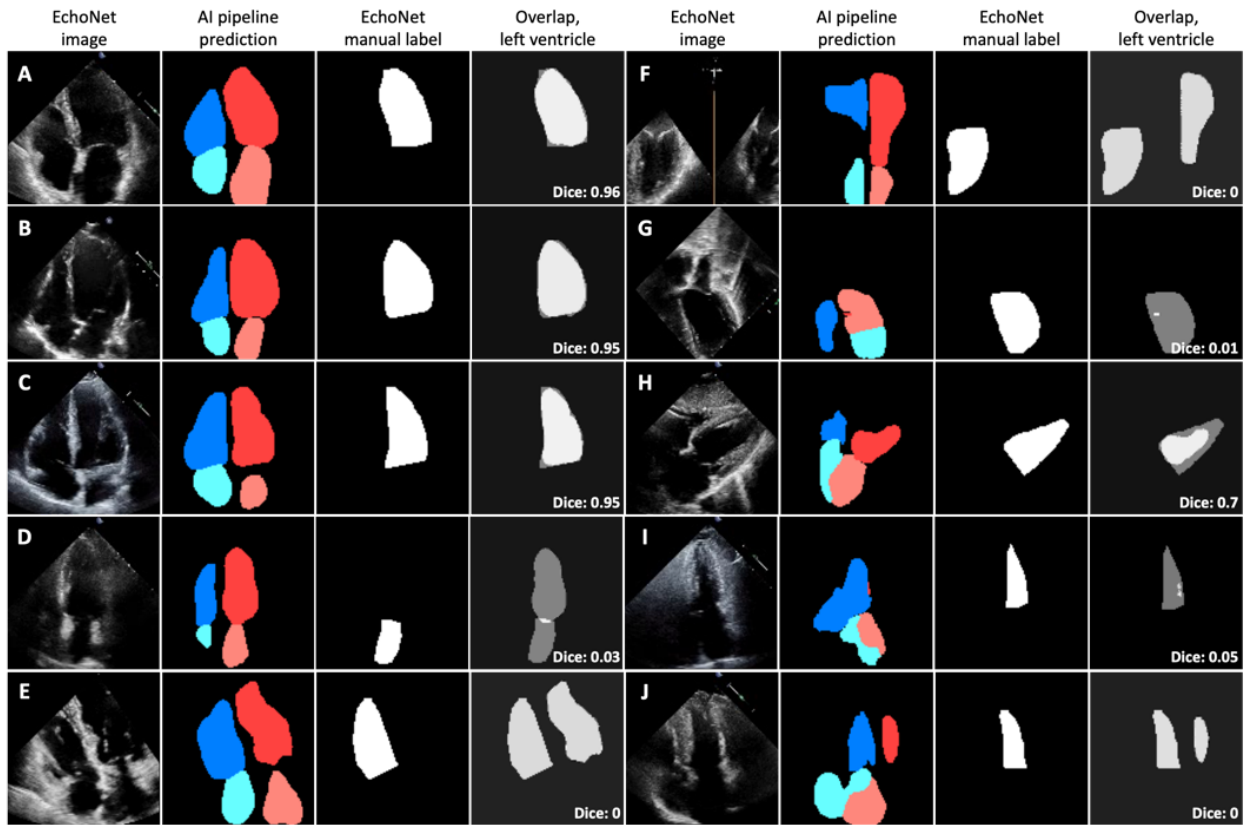


Supplemental Figure 4. Examples of A4C images at each step of the AI pipeline. (A) shows a typical good-quality A4C image: the initial weak label (step B1) segment the chambers poorly

but are corrected through successive steps of the pipeline to final prediction (step B4). In (B), a filling defect from an LV thrombus (white arrow) was still present in the final segmentation. In (C), segmentation performs well despite presence of a pericardial effusion (blue arrowheads). In (D), segmentation performs well despite massive RA and RV enlargement and septal flattening due to pulmonary hypertension. In (E), segmentation performs well despite left atrial enlargement and a zoomed-in view. Ventricles in zoomed-in views like this would be excluded from clinical calculations, while the atria would be used. A4C = apical 4-chamber, LV = left ventricle, RA = right atrium, RV = right ventricle.



Supplemental Figure 5. Examples of SAX images at each step of the AI pipeline. (A) shows a typical good-quality SAX image: the initial weak label (step C1) is a simple circle, but good segmentations are built up through successive steps of the pipeline to final prediction (step C4). In (B), final segmentation prediction is reasonable despite a slightly off-axis SAX. In (C), segmentation performs reasonably despite pulmonary hypertension and septal flattening, but the true degree of septal flattening is blunted in the final prediction. In (D), segmentation performs poorly due to a technically difficult image with dropout in the area of the septum, but still recovers a final prediction despite no prediction in step C2. SAX = short-axis mid.



Supplemental Figure 6. AI pipeline performance on A4C images from an external dataset.

This dataset had only A4C images, and manually annotated clinical labels for only the left ventricle available. Dice scores (“Overlap, left ventricle”) between the AI pipeline’s LV segmentation (“AI pipeline prediction,” red) and the manual LV segmentation (“EchoNet manual label”) are shown. Average Dice score between AI pipeline and manual labels was 0.83 over more than 20 thousand images. This average Dice includes examples where AI pipeline matched manual label well with high per-image Dice scores (A-C); examples where the AI pipeline was correct, but the manual label incorrectly labeled the left atrium (D) or the right ventricle (E) leading to extremely low per-image Dice scores. Overall performance also included image view types in the external dataset that were not part of the AI pipeline training, such as split view (F), inverted view (G), and subcostal view (H). Finally, it included rare examples where the manual label was correct, and the AI pipeline failed (I-J). (In the AI pipeline, such images would fail quality control and not be used for measurements calculation.)

References

1. Madani A, Arnaout R, Mofrad M, Arnaout R. Fast and accurate view classification of echocardiograms using deep learning. *npj Digital Med.* 2018;1(1):6. doi:10.1038/s41746-017-0013-1
2. Chinn EM, Arora R, Arnaout R, Arnaout R. ENRICH: Exploiting Image Similarity to Maximize Efficient Machine Learning in Medical Imaging. *medRxiv*. Published online May 25, 2021:2021.05.22.21257645. doi:10.1101/2021.05.22.21257645
3. Ronneberger O, Fischer P, Brox T. U-Net: Convolutional Networks for Biomedical Image Segmentation. In: Navab N, Hornegger J, Wells WM, Frangi AF, eds. *Medical Image Computing and Computer-Assisted Intervention – MICCAI 2015*. Lecture Notes in Computer Science. Springer International Publishing; 2015:234-241. doi:10.1007/978-3-319-24574-4_28
4. Xie S, Tu Z. Holistically-nested edge detection. In: *Proceedings of the IEEE International Conference on Computer Vision*. ; 2015:1395-1403.
5. Zhang C, Bengio S, Hardt M, Recht B, Vinyals O. Understanding deep learning (still) requires rethinking generalization. *Communications of the ACM*. 2021;64(3):107-115.
6. Arpit D, Jastrzębski S, Ballas N, et al. A closer look at memorization in deep networks. In: *International Conference on Machine Learning*. PMLR; 2017:233-242.
7. Yu S, Chen M, Zhang E, et al. Robustness study of noisy annotation in deep learning based medical image segmentation. *Phys Med Biol.* 2020;65(17):175007. doi:10.1088/1361-6560/ab99e5
8. Liu S, Niles-Weed J, Razavian N, Fernandez-Granda C. Early-learning regularization prevents memorization of noisy labels. *Advances in neural information processing systems*. 2020;33:20331-20342.
9. Liu S, Liu K, Zhu W, Shen Y, Fernandez-Granda C. Adaptive early-learning correction for segmentation from noisy annotations. In: *Proceedings of the IEEE/CVF Conference on Computer Vision and Pattern Recognition*. ; 2022:2606-2616.
10. Triguero I, García S, Herrera F. Self-labeled techniques for semi-supervised learning: taxonomy, software and empirical study. *Knowledge and Information systems*. 2015;42(2):245-284.
11. Lang RM, Badano LP, Mor-Avi V, et al. Recommendations for Cardiac Chamber Quantification by Echocardiography in Adults: An Update from the American Society of Echocardiography and the European Association of Cardiovascular Imaging. *Journal of the American Society of Echocardiography*. 2015;28(1):1-39.e14. doi:10.1016/j.echo.2014.10.003

12. Arnaout R, Curran L, Chinn E, Zhao Y, Moon-Grady A. Deep-learning models improve on community-level diagnosis for common congenital heart disease lesions. *arXiv preprint arXiv:180906993*. Published online 2018.
13. Shibin Wu, Qingsong Zhu, Yaoqin Xie. Evaluation of various speckle reduction filters on medical ultrasound images. In: *2013 35th Annual International Conference of the IEEE Engineering in Medicine and Biology Society (EMBC)*. IEEE; 2013:1148-1151.
doi:10.1109/EMBC.2013.6609709
14. Roerdink JB, Meijster A. The watershed transform: Definitions, algorithms and parallelization strategies. *Fundamenta informaticae*. 2000;41(1-2):187-228.
15. Yuen HK, Princen J, Illingworth J, Kittler J. Comparative study of Hough transform methods for circle finding. *Image and vision computing*. 1990;8(1):71-77.
16. Ouyang D, He B, Ghorbani A, et al. Echonet-dynamic: a large new cardiac motion video data resource for medical machine learning. In: *NeurIPS ML4H Workshop: Vancouver, BC, Canada*. ; 2019.